Proceedings of the 2004 IEEE
International Conference on Robotics & Automation
New Orleans, LA • April 2004

The DLR Multisensory Hand-Guided Device: The Laser Stripe Profiler

K. H. Strobl, W. Sepp, E. Wahl, T. Bodenmüller, M. Suppa, J. F. Seara, and G. Hirzinger

Institute of Robotics and Mechatronics
German Aerospace Center DLR
82230 Wessling, Germany
Klaus.Strobl@dlr.de

***Abstract*— This paper presents the DLR Laser Stripe Profiler as a component of the DLR multisensory Hand-Guided Device for 3D modeling. After modeling the reconstruction process, we propose a *novel method for laser plane self-calibration* based on the assessment of the deformations the miscalibration leads to. In addition, the requirement for absence of optical filtering implies the development of a *robust stripe segmentation algorithm*. Experiments demonstrate the validity and applicability of the approaches.**

I. Introduction

There is currently a very strong need for building 3D models in order to inspect, document, and reproduce objects in the fields of industry, medicine, and entertainment. Specific applications are reverse engineering, telepresence, and virtual reality. 3D models are often gained through computer-aided vision, since vision provides more information about the immediate environment than any other type of sensing technique. 3D modeling is the way for machines to *see*, i.e. to segment and localize objects, since the real dimensions and shape of the data are preserved – unlike in 2D images. Besides, powerful algorithms gradually complement 3D modeling aiming to perform segmentation and classification in a better way than with 2D images [1]. This paper deals with one of the most common methods of 3D modeling, the *active optical triangulation*.

In particular, we present a single laser stripe profiler. Special characteristics of our profiler with respect to others are: on the one hand, the absence of optical filtering on the CCD camera – this implies robust image processing methods. On the other hand, the need for a simple and precise laser plane calibration method in order to keep costs low.

The usual way of dealing with laser plane calibration requires precise calibration targets, or rather precise positioning of them, in order to identify known world points within the projected image points, and then reconstructing the relative pose of the laser plane. Nonetheless, it is expensive to build such reference artifacts and, what is more, the errors certainly made during their construction can not be eventually included in measurement error estimations. In addition, most of these methods use fiducial marks or *blob*s (***b**inary **l**arge **ob**jects*) – integrating intensity for centroid estimation – or just corner features for detecting these points [2].

J. F. Seara is with the Institute of Automatic Control Engineering *LSR* at the Technische Universität München *TUM*.

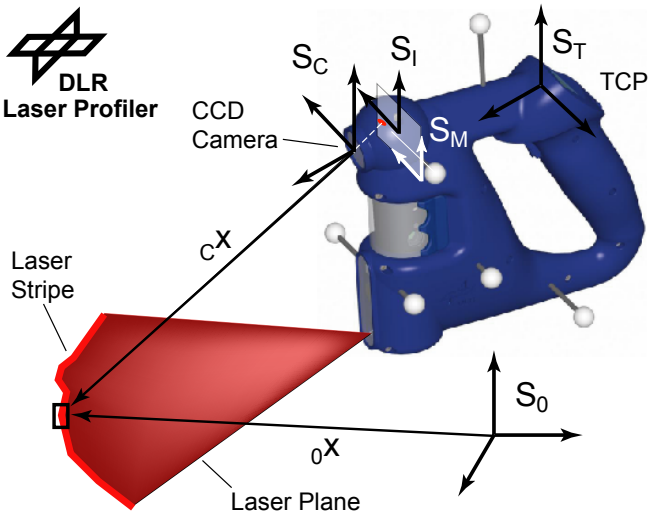

Fig. 1
The DLR Hand-Guided Device – in detail the Laser Profiler.

Neither fiducial marks because of the perspective projection, nor corner features because these are a chronic problem for 3D scanning [3], seem to be appropriate for a calibration stage. The use of point features by means of peak-detection algorithms [4] seems therefore much more convenient. Further approaches use stereo–vision for locating the stripes in the space [5] – these approaches do not suffer from these problems, but rely strongly on the accuracy of both camera calibrations obtained in advance. Inspired by the self-calibration method of Jokinen in Ref. [6], we propose a novel method for laser plane self-calibration based on the assessment of the deformations due to miscalibration.

This article is organized as follows: after giving in Section II an outline of the DLR multisensory hand-guided device, the formulation of the perception process for the laser profiler is presented in Section III. This formulation represents the starting point for the novel calibration process presented in Section IV. The required image processing methods are exposed in Section V – both Sections IV and V cover the main contributions of this work. Section VI demonstrates the operation of the laser profiler and validates the accuracy of the calibration process. The article closes in Section VII with concluding remarks and an outlook on future contributions.

0-7803-8232-3/04/$17.00 ©2004 IEEE

II. The DLR Multisensory Hand-Guided Device

When gaining *complete* 360° 3D models through imaging system transport methods [7], two general but oppositional approaches are common. On the one hand, one can acquire data from arbitrary unknown positions, and then merge these 2.5D views to a single 3D model by registering them. On the other hand, one can additionally measure the pose of the sensor which collects the data in order to represent the results directly in the world frame S_0.

The hand-guided system developed at DLR realizes the second approach. Hand-guided systems present advantages when measuring complex objects, since it is easy to select the area to be scanned similar to using a spray can. The sensor has to be of low weight to allow a convenient and acceptable hand guidance by the user. We measure the pose of the hand-guided device by fixing it to the end-effector of a *FAROarm* comprised of 7 passive joints [8]. Alternatively, an infrared optical tracking system can be used [9]. The implementation on a robot for automatic generation of 3D models is also possible. Actually, the pose sensor refers to the ***T**ool **C**enter **P**oint* (*TCP*), and every sensor system has to be calibrated with respect to (w.r.t.) it.

Furthermore, pose and sensor data need to be synchronized w.r.t. acquisition time. Since the system's strength lies in *multisensory* 3D data acquisition, a concept for time-synchronization is required. Currently our system integrates a laser-range scanner, two cameras, and a laser stripe module for optical depth recovery, texturing, and laser profiler sensing. This paper focuses on the calibration and use of the last one. The sensors are integrated into a specially developed and easy to handle housing of low weight, cf. Fig. 1. Detailed information concerning the hand-guided device and its synchronization principle can be obtained from Ref. [10].

The given system interfaces were unified in order to simplify the inclusion of other sensors. The sensor principles can be compared, and the best one chosen for every specific task. Evading and clearing sensor weaknesses can also be accomplished. We aim robustness through data fusion.

III. The Laser Profiler Model

The fundamental principle of range sensing by optical triangulation is illustrated in Fig. 1. A focused plane of laser light illuminates a stripe when colliding with the surface of an object. A CCD camera records the reflection. Reconstruction is done by triangulation, i.e. intersecting the laser plane with the rays of sight corresponding to the laser stripe projection in the image frame S_I. As explained in last section, a complete 3D model is acquired by sweeping (i.e. *scanning*) the projected laser stripe over the surface of an object.

This principle of operation is very much alike the one of stereo–vision systems. A laser plane is used instead of a second camera in order to simplify the correspondence problem. Consequently, the major obstacle of stereo–vision in 3D modeling – the computational requirements – can be overcome.

In this section both the projection model and the reconstruction process for surface points are presented.

A. Pose Sensor Model

In order to provide generality for this work, the 6D pose sensor will be modeled as a homogeneous transformation from the world frame S_0 into the *TCP* frame S_T:

$$ {}_T\tilde{\boldsymbol{x}} = {}^T\boldsymbol{T}_0 \, {}_0\tilde{\boldsymbol{x}} \,, \tag{1} $$

where ${}_0\tilde{\boldsymbol{x}}$ represents the *homogeneous* form of the position coordinates of a 3D point ${}_0\boldsymbol{x}$ in S_0.

B. Camera Model

In this section the modeling of the transformation from S_T into the image memory frame S_M is described – see Fig. 1. The first step is the transformation from S_T into the camera frame S_C, which is composed of the external camera parameters of the calibration process – cf. Section IV-A:

$$ {}_C\tilde{\boldsymbol{x}} = {}^C\boldsymbol{T}_T \, {}_T\tilde{\boldsymbol{x}} \quad with \quad {}^C\boldsymbol{T}_T = \begin{bmatrix} {}^C\boldsymbol{R}_T & {}_C\boldsymbol{t} \\ \boldsymbol{0}^t & 1 \end{bmatrix} . \tag{2} $$

On the basis of the pinhole camera model, and employing the camera internal parameter f (focal distance), the *undistorted* image coordinates ${}_I\boldsymbol{m}_u$ in the image frame S_I are

$$ {}_I\boldsymbol{m}_u = \begin{bmatrix} {}_Iu_u \\ {}_Iv_u \end{bmatrix} = -f/{}_Cz \begin{bmatrix} {}_Cx \\ {}_Cy \end{bmatrix} . \tag{3} $$

Merging Eqs. (2) and (3):

$$ s \, {}_I\widetilde{\boldsymbol{m}}_u = \boldsymbol{P} \, {}_T\tilde{\boldsymbol{x}} \tag{4} $$

where the perception matrix $\boldsymbol{P}$ can be written as follows:

$$ \boldsymbol{P} = \left(\begin{array}{ccc|c} -f\,r_{11} & -f\,r_{12} & -f\,r_{13} & -f\,t_x \\ -f\,r_{21} & -f\,r_{22} & -f\,r_{23} & -f\,t_y \\ r_{31} & r_{32} & r_{33} & t_z \end{array} \right) = \begin{pmatrix} \boldsymbol{q}_1^t & q_{14} \\ \boldsymbol{q}_2^t & q_{24} \\ \boldsymbol{q}_3^t & q_{34} \end{pmatrix} $$

where t_i and r_{ij} are the components of ${}_C\boldsymbol{t}$ and ${}^C\boldsymbol{R}_T$ respectively. The free parameter s represents the underdetermined nature of the perception process for this one pinhole camera.

The *undistorted* image metric coordinates ${}_I\boldsymbol{m}_u$ differ from the ones expressed in S_M due to both the lens distortion and the digitizing process. In this work, a bivariate third-degree polynomial is supposed to cope with image correction, turning the *undistorted* image metric coordinates ${}_I\boldsymbol{m}_u$ into *distorted* image pixel coordinates in the memory frame ${}_M\boldsymbol{m}_d$. This representation covers a variety of typical lens distortion phenomena beyond the radial distortion assumption [11]. In addition, this approach makes the relation between S_I and S_M transparent, as both the distortion and the digitizing parameters remain combined in the coefficients.

C. Laser Plane Model

The laser plane is a laser beam that is spread by passing it through a cylindrical lens. Both the laser illuminant and the camera are rigidly integrated, i.e. the plane normal vector ${}_T\boldsymbol{n}$ and its distance ${}_Td$ w.r.t. the *TCP* do not vary. Hence we have:

$$ \left[{}_T\boldsymbol{n}^t \; {}_Td \right] {}_T\tilde{\boldsymbol{x}} = 0 \,. \tag{5} $$

D. Projection from 3D to 2D

Mapping from a 3D point in S_0 to its representation in S_M comprises then Eqs. (1), (4), and the proposed distortion and digitizing model, for any point illuminated by the laser plane described in Eq. (5).

E. Reconstruction from 2D to 3D

For purposes of 3D world modeling, the interesting transformation is however the inverse one, and moreover its precision. The objective is to *estimate* the world coordinates ${}_0\hat{\boldsymbol{x}}$, given the image pixel coordinates of a point illuminated directly by the laser plane ${}_M\boldsymbol{m}$, the current pose of the *TCP* ${}^T\boldsymbol{T}_0$, and the calibration parameters of both camera and laser plane.

Assuming the segmentation problem is solved – refer to Section V, the procedure is to transform image pixel coordinates from S_M backwards into S_0 by means of the inversion of the distortion and digitizing model and Eqs. (4), (1), taking into account Eq. (5).

Since the distortion and digitizing model can not be inverted in closed form, we approximate it using *image rectification*[1]. In this way, the coordinate mapping represented in the distortion model turns into the linear relation

$$\begin{bmatrix} {}_M\hat{u}_u \\ {}_M\hat{v}_u \end{bmatrix} = \begin{bmatrix} s_x & 0 & {}_Mu_p \\ 0 & s_y & {}_Mv_p \end{bmatrix} \begin{bmatrix} {}_I\hat{u}_u \\ {}_I\hat{v}_u \\ 1 \end{bmatrix}, \tag{6}$$

where ${}_Mu_p$ and ${}_Mv_p$ are the image pixel coordinates of the principal point, and s_x and s_y the distortion-free scaling factors – from ${}_I\boldsymbol{x}$ to ${}_M\boldsymbol{x}$ and from ${}_I\boldsymbol{y}$ to ${}_M\boldsymbol{y}$ respectively. The latter denote the relation between the unit distance between adjacent *pel*s (***p**icture **el**ement*s) in S_M and the unit distance between adjacent *sel*s (***s**ensing **el**ement*s) in S_I. Finding ${}_I\widehat{m}_u$:

$$\begin{bmatrix} {}_I\hat{u}_u \\ {}_I\hat{v}_u \end{bmatrix} = \begin{bmatrix} ({}_M\hat{u}_u - {}_Mu_p)/s_x \\ ({}_M\hat{v}_u - {}_Mv_p)/s_y \end{bmatrix}. \tag{7}$$

When solving for ${}_T\hat{\boldsymbol{x}}$, the system of Eqs. (4), (5) can be written as

$$\left.\begin{aligned} ({}_I\hat{u}_u\,\boldsymbol{q}_3^t - \boldsymbol{q}_1^t)\,{}_T\hat{\boldsymbol{x}} &= q_{14} - {}_I\hat{u}_u\,q_{34} \\ ({}_I\hat{v}_u\,\boldsymbol{q}_3^t - \boldsymbol{q}_2^t)\,{}_T\hat{\boldsymbol{x}} &= q_{24} - {}_I\hat{v}_u\,q_{34} \\ {}_T\boldsymbol{n}^t\,{}_T\hat{\boldsymbol{x}} &= -{}_Td \end{aligned}\right\} \tag{8}$$

representing a linear equation system in the form $\widehat{\boldsymbol{F}}\,{}_T\hat{\boldsymbol{x}} = \hat{\boldsymbol{b}}$. In all practical cases this system has the solution ${}_T\hat{\boldsymbol{x}} = \widehat{\boldsymbol{F}}^{-1}\hat{\boldsymbol{b}}$. The last step is its representation in S_0:

$$\begin{bmatrix} {}_0\hat{\boldsymbol{x}} \\ 1 \end{bmatrix} = {}^0\boldsymbol{T}_T \begin{bmatrix} \widehat{\boldsymbol{F}}^{-1}\,\hat{\boldsymbol{b}} \\ 1 \end{bmatrix}. \tag{9}$$

IV. The Laser Profiler Calibration

The accuracy of the laser profiler depends directly on the errors in the calibration process. It must be calibrated with very high precision both in geometric and optic issues. Next the parameters involved in the sensor model presented in the last section are estimated.

[1] *Image rectification* exploits the distortion parameters identified in the calibration process – Section IV-A – and geometrically transforms an input image such that distortion is eliminated in S_M and the transformation from S_M into S_I becomes linear.

A. Camera Calibration

Camera calibration is the process of determining the internal camera geometric and optical characteristics (*intrinsic parameters*) and the 6D pose of S_C w.r.t. S_T (*extrinsic parameters*). For laser stripe profilers, this is a cumbersome process, since they usually suffer from heavily filtered cameras in order to simplify the stripe segmentation process – see Section V. In our work, both because of this inconvenience, and having in mind to allow the gathering of further data from our hand-guided device (e.g. texturing or visual stereo sensing), it was a requirement to develop the profiler without optical bandpass filters.

In line with the camera model presented in Section III-B, the parameters ${}^C\boldsymbol{T}_T$, f, a_i, and b_i where i=0..9, are estimated by means of the calibration toolbox CALLAB [12]. This X-WINDOW based software package calibrates stereoscopic hand-eye cameras from a series of stereo–images of a well defined calibration grid and a quite accurate estimation of ${}^T\boldsymbol{T}_0$ for every image. In addition, CALLAB provides extensive statistical analysis of residual errors.

B. Laser Plane Calibration

Laser plane calibration is the process of determining the relative pose of the laser plane w.r.t. S_C (or S_T). This is a particularly critical point for triangulation, since its miscalibration leads to misalignments and warpage effects in the scanned surfaces related to the scanning poses – cf. Fig. 8.

As already explained in Section I, we propose a novel method for laser plane self-calibration based on the assessment of the deformations the miscalibration leads to. In his work [6], Jokinen's calibration approach focuses on matching maps, searching for shape correspondences – the method is based on previous research in registration algorithms. We propose here a method that focuses on *correcting* the resulting maps, rather than on *matching* them, reaching in this way a much simpler and swifter formulation. Moreover, this method does not require any complicated calibration target.

When locating the laser plane, i.e. estimating the parameters ${}_T\boldsymbol{n}$ and ${}_Td$ in Eq. (5), there are three *independent **D**egrees **o**f **F**reedom* (*DoF*) to be identified. Here the spherical-polar coordinates in S_C are used: roll ${}_C\alpha$, pitch ${}_C\beta$, and distance ${}_Cd$, $/\,{}_C\boldsymbol{\Omega}=\{{}_C\alpha,\,{}_C\beta,\,{}_Cd\}$. For any roughly *estimated* laser plane pose ${}_C\widehat{\boldsymbol{\Omega}}$, the errors ${}_C\varepsilon_\alpha$, ${}_C\varepsilon_\beta$, and ${}_C\varepsilon_d$ occur. These errors cause deformations on the estimated surface for every scanning movement of the hand-guided device. These deformations include from simple scaling errors (typically when having high ${}_C\varepsilon_d$), up to convex/concave warped deformations (typically when having high ${}_C\varepsilon_\beta$ – cf. Fig. 2), or even irregularly warped results (both with high ${}_C\varepsilon_\alpha$ and with a mixture of them all).

The self-calibration method works as follows: the reconstruction process runs with some initial laser plane calibration parameters ${}_C\widehat{\boldsymbol{\Omega}}_o$, roughly estimated a priori. The proposed method exploits the distortions caused in the reconstruction process when scanning surfaces. As calibration surface we use *a plane* of unknown pose, both in order to avoid the construction of a complex calibration target and due to the fact

that a plane has the geometrical shape that can be straightened out in the easiest way. In the process, all the sensor poses $\Upsilon = {}^{0}\boldsymbol{T}_{T\{i=1..n\}}$ and two image points nearby the ends of every stripes $\Phi = {}_{M}\boldsymbol{m}_{\{i=1..n\}\{1..2\}}$ are stored for every image i. Both poses and image points yield to $2n$ world points ${}_{0}\hat{\boldsymbol{p}}_{i\{1,2\}} = \boldsymbol{p}\left({}^{0}\boldsymbol{T}_{Ti},\ {}_{M}\boldsymbol{m}_{i\{1,2\}},\ {}_{C}\widehat{\boldsymbol{\Omega}}\right)$ – cf. Eq. (9). This reconstructed *pointcloud* shows unevenness when scanning from very different points of view – theoretical studies determine the ideal procedure. Subsequently, the best fitting calibration target plane for these points with normal ${}_{0}\hat{\boldsymbol{n}}_{\angle} = \boldsymbol{n}\left({}_{0}\hat{\boldsymbol{p}}_{\{1..2n\}\{1..2\}}\right)$ and distance ${}_{0}\hat{d}_{\angle} = d\left({}_{0}\hat{\boldsymbol{p}}_{\{1..2n\}\{1..2\}}\right)$ is estimated – this overdetermined problem is solved with a closed form solution in the form of *Singular Value Decomposition*. Finally, the *optimized* ($\star$) laser plane parameters ${}_{C}\widehat{\boldsymbol{\Omega}}_{\star}$ are off-line estimated: the goal is to minimize the mean squared distance $\sigma^2_{\angle}$ of every reconstructed points ${}_{0}\hat{\boldsymbol{p}}_{i\{1,2\}}$ to the best fitting plane. This can be expressed as:

$$ {}_{C}\widehat{\boldsymbol{\Omega}}_{\star} = \arg\min_{{}_{C}\widehat{\boldsymbol{\Omega}}} \sigma^2_{\angle}\left(\Upsilon,\ \Phi,\ {}_{C}\widehat{\boldsymbol{\Omega}}\right) \quad , \tag{10} $$

$$ \sigma^2_{\angle} = \sum_{i=1}^{2n} \left({}_{0}\hat{d}_{\angle} - {}_{0}\hat{\boldsymbol{n}}^{t}_{\angle}\ {}_{0}\hat{\boldsymbol{p}}_{i\{1,2\}}\right)^2 . \tag{11} $$

The *Nelder-Mead Simplex* method has been implemented for numerical optimization. To recapitulate, the laser plane parameters are adapted in such a way that in the end the scanned surface becomes as flat as possible.

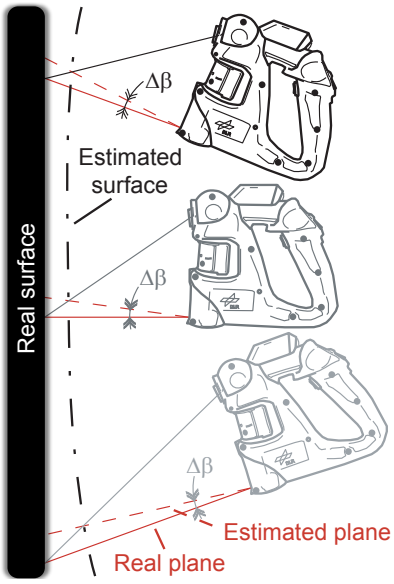

Fig. 2

LASER PITCH ORIENTATION MISCALIBRATION CONSEQUENCES.

Fig. 3 shows the 2D cost matrix representing the achieved flatness (i.e. $\sigma^2_{\angle}$) for different laser plane poses ${}_{C}\boldsymbol{\Omega}$ with fixed ${}_{C}d = {}_{C}d_c$ and variable ${}_{C}\alpha$ and ${}_{C}\beta$. ${}_{C}\boldsymbol{\Omega}_c = \{{}_{C}\alpha_c,\ {}_{C}\beta_c,\ {}_{C}d_c\}$ are the actual laser pose parameters. The figure shows the robustness of the method for any reasonable initial ${}_{C}\widehat{\boldsymbol{\Omega}}_o$, provided the laser plane intersects the image rays in the camera view direction. It is worth noting that for distances ${}_{C}\hat{d} \neq {}_{C}d_c$ the optimal orientation parameters ${}_{C}\hat{\alpha}_{\star}$ and ${}_{C}\hat{\beta}_{\star}$ vary slightly from the actual ones ${}_{C}\alpha_c$ and ${}_{C}\beta_c$, particularly ${}_{C}\hat{\beta}_{\star}$. This is due to the fact that a variation in ${}_{C}\hat{\beta}_{\star}$ compensates for an erroneous ${}_{C}\hat{d}$ when scanning with constant orientation and distance of the profiler w.r.t. the calibration plane. Owing to the very different poses made in the calibration process, this does not yield any problem for this optimization algorithm, and this compensation mechanism does not get the flatness the actual parameters do.

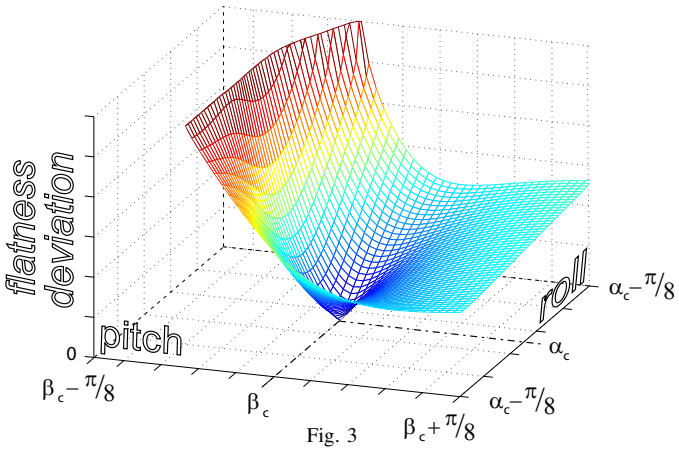

Fig. 3

FLATNESS DEVIATION OF THE RECONSTRUCTED PLANE WITH ${}_{C}d = {}_{C}d_c$.

V. LASER STRIPE SEGMENTATION

Besides the calibration process, a decisive factor for ranging accuracy is obviously the segmentation of the laser stripe projection (detection of the center points of the *red* laser stripe in the image in S_M – cf. Fig. 4), since the resulting image pixel coordinates in S_M are the principal inputs to the reconstruction process – see Section III-E.

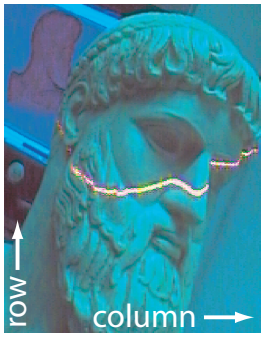

Fig. 4

STRIPE SEGMENTATION.

In order to widen the range of objects to be scanned, the image processing algorithms do not have precise a priori knowledge about the shape of the laser outlines. This fact may yield erroneous results. For instance, in the case of specular reflections or red light sources, a simple segmentation algorithm would detect them erroneously as laser projections. Therefore, different measures must be taken to reduce these kinds of failures. Another point is that the profiler camera does not have any optical filter, so that the segmentation process becomes complicated.

The first point to be considered in order to achieve an optimal performance is the adjustment of some physical parameters of the camera. On this matter, in order to avoid both desyncronizations and radiometric distortions [13], only the even fields of the interlaced images are used. Focus and aperture have to be chosen appropriately. In addition, in order to maximize both the range of view and the range precision using single image fields, the camera and the laser are arranged

such that the projected stripes are approximately *perpendicular* to the image rows, cf. Fig. 4.

The implemented approach is based on four image processing stages. The approach is as follows: image i is processed row by row. For each row r, different laser stripes may be detected by means of *Step 1)*. *Steps 2)* and *3)* validate the result and, in the affirmative, *Step 4)* estimates the center point of the stripe ${}_M\boldsymbol{m}_{rsi}$ where s numbers different results in the same row r and image i.

1) Stripe edges detection: The algorithm for detecting both upper and lower edges of the stripe is based on the *Sobel* Filter. It approximates absolute gradient magnitudes at each image point ${}_M\boldsymbol{m}$ and, in addition, filters possible noises. First, the red component of the image i is extracted. Second, the convolution of the *Sobel* kernel in the resulting image emphasizes the horizontal edges of the laser stripe – these are outlined w.r.t. the background owing to both the tight focusing and the strong brightness of the laser beam. On the basis of the resulting image, in every image row r upper and lower edges of multiple stripes can be detected when setting a threshold value for this absolute derivative (i.e. brightness). Nevertheless, two additional validation stages are included in order to exclude misclassified stripes (e.g. in the case of specular reflections):

2) Color validation: To validate the detected stripe, the pixel color values between two adjacent edges of *Step 1)* are examined. For this purpose, a ***L**ook-**U**p **T**able* (*LUT*) is online generated to decide whether an image pixel color value belongs to the *background colorsubspace* or to the laser stripe one. It is created as follows: a series of pictures $\boldsymbol{I}_i$ are taken from the environment prior to the scanning process with the laser beam turned off. Here $\boldsymbol{I}_i = \{\boldsymbol{c}_0, \boldsymbol{c}_1, \ldots, \boldsymbol{c}_n\}$ where $\boldsymbol{c}_j = (\mathcal{R}, \mathcal{G}, \mathcal{B}) \in [0,31][0,63][0,31]$. All perceived color values are stored online in a preliminary background *LUT*

$$\widetilde{\boldsymbol{bcs}}\,(\mathcal{R},\mathcal{G},\mathcal{B}) = \begin{cases} 1 & \text{if} \quad \exists\, i : (\mathcal{R},\mathcal{G},\mathcal{B}) \in \boldsymbol{I}_i \;\cup\; \mathcal{R}=0 \\ 0 & \text{if} \quad \text{else} \end{cases} .$$

The set indices match up then with background (including objects) color values. However, this assertion may not be reciprocal, i.e. there may be background color values not yet set in the former indices in relation to the limited diversity of the gathered images. In order to ensure completeness an *LUT* named $\boldsymbol{bcs}$ is created based on the assumption that laser stripe color values are supposed to hold higher red components:

$$\boldsymbol{bcs}\,(\mathcal{R},\mathcal{G},\mathcal{B}) = \begin{cases} 1 & \text{if} \quad \exists\, \mathcal{R}' \geq \mathcal{R} - \Delta\mathcal{R} : \widetilde{\boldsymbol{bcs}}\,(\mathcal{R}',\mathcal{G},\mathcal{B}) = 1 \\ 0 & \text{if} \quad \text{else} \end{cases}$$

where $\Delta\mathcal{R}$ represents a red offset[2]. Fig. 5 shows an example of the set $\widetilde{\boldsymbol{bcs}}$ indices. The resulting stripes of *Step 1)* are accepted whenever there are laser pixel color values within their upper and lower edges, i.e. when their respective $\boldsymbol{bcs}$ entry is *not* set. This method copes very well with the problem of specular reflections. In addition, this method provides *robustness* and *flexibility* against changing lighting conditions.

[2]The reason for this offset is the diffuse radiation the laser sends out to the environment when functioning due to impurities in the spreading cylindrical lens.

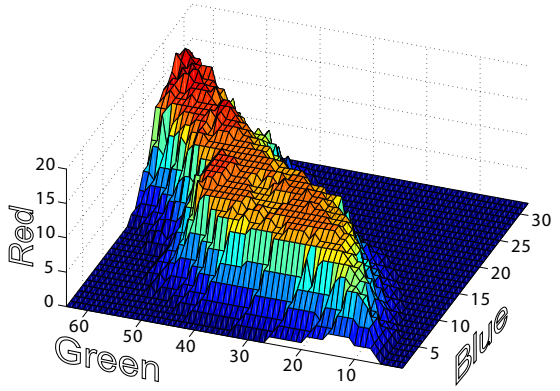

Fig. 5

$\mathcal{RGB}565$ LOOK-UP TABLE.

FOR RED VALUES ABOVE THIS MESH, STEP *2)* IS FULFILLED.

3) Width validation: This second validation focuses on the problem of the specular reflections caused by the laser itself, most likely recognized as stripes by the first steps. This method accepts a laser stripe whenever the pixel width of the stripe is within a certain range – the width of the stripe depends on the measuring distance, the projection angle, and the surface reflection properties. In order not to be conservative when defining this interval, experiments have been performed to identify the biggest and the smallest stripe widths for every projected point in S_M – see Fig. 6. These were then stored in an *LUT* and remain valid for the whole operation of the profiler. In addition, this method corrects some erroneous measurements when coping with object corners [14].

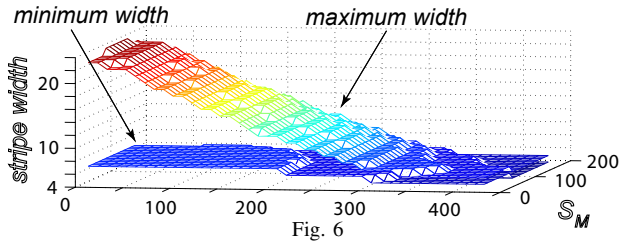

Fig. 6

MAXIMUM AND MINIMUM ALLOWED WIDTH FOR EVERY PROJECTED STRIPE POINT ${}_M\boldsymbol{m}$.

4) Center of stripe estimation: Once a valid stripe projection has been found, its projection center point is determined. This is estimated to sub-pixel precision (to within a fraction of a pixel) by means of the center of mass method over the red channel of the image. The precisions achieved are comparable with the ones reached with other advanced methods like Gaussian approximation [4]. Besides, the saturated brightness values rule the latter out – saturation is very likely for non-filtered cameras which capture laser reflections. Once an image point ${}_M\boldsymbol{m}_{rsi}$ is available, it gives then raise to a 3D coordinate ${}_0\boldsymbol{x}$, making use of Eq. (9).

In addition to the taken measures, outliers-rejecting algorithms can be implemented, either based on an error-model or rejecting features which generate range values depending on the camera position. There are also other kinds of segmentation errors characteristics of the profiler operation related to occlusion and obscuration events [14].

VI. Results

Next the operation of the laser profiler is shown. A point is made regarding the calibration precision.

A. *Gaining* complete *models*

The profiler was used to capture a complete model of the bust of Fig. 4. The scanning speed is limited by the desired density of data. At a distance of $30\,cm$, a point density of $2\,mm$ in the stripe direction is achieved owing to the camera even field resolution. The same density in the sweep direction is achieved at $5\,cm/s$, using a PAL camera. Fig. 7 shows the resulting 3D model eventually meshed with a grid the size of $1.5\,mm$.

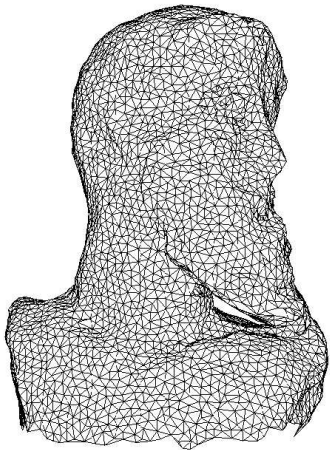

Fig. 7
Meshed 3D model of Zeus.

B. *Assessment of the Calibration Precision*

In order to show the importance of the laser plane calibration accuracy and get an idea of the actual precision after calibrating the laser plane with the method presented in Section IV-B, we next present a typical example for showing the errors of miscalibrated systems. Fig. 8 shows some scanning results over a small cardboard box focused orthogonally to one of its corners. The box was scanned three times: the first orthogonally to the top (1), the second orthogonally to a side (2), and the third orthogonally to the corner edge and in the direction of the bisector of the angle formed between these two sides (3). This particular procedure facilitates the assessment of the reconstruction errors. Fig. 8 (a) shows the profile under correct calibration results according to Section IV-B. The profiler exhibits a range precision in the sub-millimeter domain. Fig. 8 (b) shows the effect of slightly modified laser plane parameters to the latter – the laser plane pose has been erroneously estimated with $\varepsilon_\beta = 1^o$. Misalignments and warpage appear for this small calibration error. This result gives an idea of both the achieved calibration accuracy and its precision.

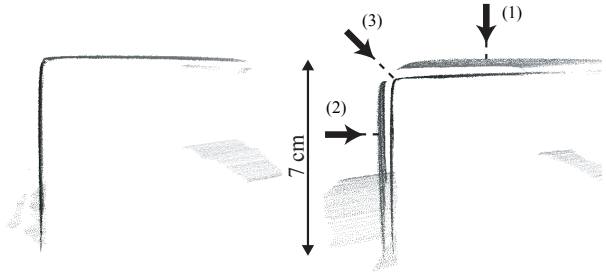

Fig. 8
Two sides of a cardboard box scanned with optimized (A) and slightly erroneous (B) laser plane calibration parameters ${}_C\boldsymbol{\Omega}$.

VII. Conclusion and Future Work

In this article we report on the DLR Laser Stripe Profiler. The main contributions of this article are: on the one hand, the proposition of a *novel self-calibration method* based on the *correction* of the deformations caused by miscalibration of the laser plane. On the other hand, a *robust stripe segmentation algorithm* is presented. The absence of optical filtering when gathering laser stripe images accounts for this robust *software-based* segmentation. The excellent operation of these two methods has been demonstrated by 3D modeling of real world complex objects.

In order to improve the estimation accuracy in these stochastical processes, statistical methods have to be applied, from which *meshing* and *exploration* tasks can benefit [15]. Some work in this direction, together with a parameterized analytical error-model of the laser stripe profiler shall be reported next.

Acknowledgment

The authors would like to thank Dr. Friedrich Lange and Dr. Heiko Hirschmüller for their helpful suggestions. This work was partly supported by the Bayerische Kompetenznetzwerk für Mechatronik *BKM*.

References

[1] E. Wahl, U. Hillenbrand, and G. Hirzinger, "Surflet-Pair-Relation Histograms: A Statistical 3D-Shape Representation for Rapid Classification," in *3-D Digital Imaging and Modeling 3DIM*, Banff, Canada, October 2003. 1

[2] A. McIvor, "Nonlinear Calibration of a Laser Stripe Profiler," *Optical Engineering*, vol. 41, no. 1, pp. 205–212, January 2002. 1

[3] B. Curless and M. Levoy, "Better Optical Triangulation through Space-time Analysis," in *Proc. of the Int. Conf. on Computer Vision ICCV*, Cambridge, MA, June 1995, pp. 987–994. 1

[4] E. Trucco, R. B. Fisher, A. W. Fitzgibbon, and D. K. Naidu, "Calibration, Data Consistency and Model Acquisition with a 3-D Laser Striper," *Int. Journal of Computer Integrated Manufacturing*, vol. 11, no. 4, pp. 293–310, 1998. 1, 5

[5] G. Taylor, L. Kleeman, and Å. Wernersson, "Robust Colour and Range Sensing for Robotic Applications Using a Stereoscopic Light Stripe Scanner," in *Proc. of the IEEE/RSJ Int. Conf. on Intelligent Robots and Systems IROS*, Lausanne, Switzerland, October 2002, pp. 86–91. 1

[6] O. Jokinen, "Self-Calibration of a Light Striping System by Matching Multiple 3-D Profile Maps," in *Proc. Second Int. Conf. on 3-D Digital Imaging and Modeling 3DIM'99*. Ottawa, Canada: IEEE Computer Society Press, October 1999, pp. 180–190. 1, 3

[7] F. Chen, G. M. Brown, and M. Song, "Overview of Three-Dimensional Shape Measurement using Optical Methods," *Optical Engineering*, vol. 39, no. 1, pp. 10–22, January 2000. 2

[8] FARO Technologies Inc. [Online]. Available: http://www.faro.com/ 2

[9] A.R.T. GmbH. [Online]. Available: http://www.ar-tracking.de/ 2

[10] M. Suppa and G. Hirzinger, "A Novel System Approach to Multisensory Data Acquisition," in *Proc. of the 8th Conf. on Intelligent Autonomous Systems IAS-8*, Amsterdam, The Netherlands, March 2004, in press. 2

[11] G. Konecny and G. Lehmann, *Photogrammetrie*, 4th ed. Berlin, New York: Walter De Gruyter Inc., 1985. 2

[12] CalLab: A Camera Calibration Toolbox. Institute of Robotics and Mechatronics, German Aerospace Center. [Online]. Available: http://www.robotic.de/vision/projects/Calibration/ 3

[13] G. Kamberova, "Understanding the Systematic and Random Errors in Video Sensor Data," GRASP Lab., Department of Computer and Information Science, University of Pennsylvania, Tech. Rep., 1997. 4

[14] B. Curless, "New Methods for Surface Reconstruction from Range Images," PhD Thesis, Stanford University, June 1997, Technical Report CSL-TR-97-733. 5

[15] M. Suppa, P. Wang, K. Gupta, and G. Hirzinger, "C-space Exploration Using Noisy Sensor Models," in *Proc. of the IEEE Int. Conf. on Robotics and Automation ICRA*, New Orleans, LA, USA, April 2004, in press. 6